Cross-correlation of the kinematic Sunyaev-Zel'dovich effect and 21 cm intensity mapping with tidal reconstruction

Dongzi Li,[1,2,3,*] Hong-Ming Zhu,[4,5] and Ue-Li Pen[1,3,6,7]

[1]*Canadian Institute for Theoretical Astrophysics, University of Toronto, 60 St. George Street, Toronto, Ontario M5S 3H8, Canada*
[2]*Department of Physics, University of Toronto, 60 St. George Street, Toronto, Ontario M5S 1A7, Canada*
[3]*Dunlap Institute for Astronomy and Astrophysics, University of Toronto, 50 St. George Street, Toronto, Ontario M5S 3H4, Canada*
[4]*Berkeley Center for Cosmological Physics and Department of Physics, University of California, Berkeley, California 94720, USA*
[5]*Lawrence Berkeley National Laboratory, 1 Cyclotron Road, Berkeley, California 94720, USA*
[6]*Canadian Institute for Advanced Research, CIFAR Program in Gravitation and Cosmology, Toronto, Ontario M5G 1Z8, Canada*
[7]*Perimeter Institute for Theoretical Physics, 31 Caroline Street North, Waterloo, Ontario N2L 2Y5, Canada*

(Received 2 December 2018; published 19 July 2019)

We discuss the possibility of studying diffuse baryon distributions with the kinematic Sunyaev-Zel'dovich (kSZ) effect by correlating cosmic microwave background (CMB) temperature fluctuations with density fluctuations from 21 cm intensity mapping (IM). The biggest challenge for the cross-correlation is the loss of large-scale information in IM, due to foregrounds and the zero spacing problem of interferometers. We apply the 3D tidal reconstruction algorithm to restore the lost large-scale modes, which increases the correlation by more than a factor of 3. With the predicted foreground level, we expect a $\sim 20\sigma$ detection of kSZ signal for $0.8 \lesssim z \lesssim 2.5$ with CHIME and Planck, and a $\sim 40\sigma$ detection with HIRAX and Planck. The significance can be greatly increased with next-generation facilities of higher spatial resolutions.

DOI: 10.1103/PhysRevD.100.023517

I. INTRODUCTION

For $z \lesssim 2$, a large fraction of the predicted baryon content is missing in observations. The majority of these baryons are believed to reside in the warm-hot intergalactic medium (WHIM), with typical temperatures of 10^5 K to 10^7 K [1–3]. The low density imposes difficulties for direct detection. The uncertainty in the spatial distribution of its ionization state, metallicity, and pressure leads to confusion in interpreting signals from absorption lines and soft x rays.

The kinematic Sunyaev-Zel'dovich (kSZ) effect [4–6] is a promising probe for diffuse baryon content. The kSZ signal is a secondary anisotropy in cosmic microwave background (CMB) temperature, which comes from the Doppler shift of photons induced by the radial velocity of free electrons. It has the following advantages: First of all, it receives a contribution from all the free electrons, which traces $\gtrsim 90\%$ [7] of the baryons at low redshifts. Second, the signal is mainly influenced by the electron density and the radial velocity, regardless of the temperature, pressure, and metallicity. Therefore, no extra uncertainties are involved to estimate the baryon abundance. Lastly, the radial velocity is a large-scale field, so the signal is less biased by the local environment and more indicative of the diffuse distribution. Hence, the kSZ is an unbiased probe for density fluctuations, and its strength at different angular scales can be model independently translated into baryon contents and diffuseness.

Studying the kSZ effect is challenging as it is relatively weak compared to various contaminations, such as the primary CMB, thermal SZ effects, CMB lensing, and instrumentation noises. Another consideration of kSZ is a projected signal with contributions from different redshifts mixed together. One way to mitigate the problem is to cross-correlate the CMB map with the density fluctuations from another tracer at a specific redshift. Several types of surveys have been proposed to play the role [8–12]. Galaxy spectroscopic surveys, with accurate redshift information and high angular resolution, are powerful probes of density fluctuations at low redshift for high angular scales, i.e., $\ell > 4000$ [13]. Several measurements have been made to probe the local missing baryons [14,15]. However, the survey speed and cost limit the sky coverage and depth of spectroscopic surveys. For $z \sim 1.4$–2.5 in particular, the lack of spectral lines will lead to large shot noise in the measured density field. Projected field surveys, such as

*dzli@cita.utoronto.ca

galaxy photometric surveys and gravitational lensing maps can provide a densely sampled sky up to the high redshift. However, a significant fraction of kSZ signals come from the density fluctuations along the line of sight (LOS) due to the coupling of two fields (see Sec. IV). Cross-correlating it with a survey without LOS structure will inevitably lead to suboptimal correlation and the loss of information. This situation can be changed with future high-precision photometric surveys, such as the Wide Field Infrared Survey Telescope (WFIRST) High Latitude Survey (HLS)[16]. The measured correlation between kSZ and galaxies not only reveals information about missing baryons, but it could have other cosmological impacts. For example, together with the dispersion measure from fast radio bursts, which helps break the optical depth degeneracy, the kSZ signal can be used to measure the cosmological growth rate [17].

In this paper, we discuss the possibility of cross-correlating the neutral hydrogen (HI) density field from 21 cm intensity mapping (IM) experiments with CMB anisotropies to measure kSZ signal. The 21 cm spectral lines provide accurate redshift information, and IM experiments perform fast scans of a large sky area by integrating all photons detected. In the next few years, several large-sky IM surveys are expected to release data. CHIME [18], designed to receive 21 cm signals at $z \sim 0.75$–2.5, entered the commissioning phase in 2017. HIRAX [19], targeting the same redshift but surveying the Southern sky, is expected to be commissioned in 2020. TIANLAI [20], commissioned in 2016, surveys the 21 cm sky for $z \lesssim 1.5$. And OWFA [21] will perform 21 cm IM at redshift $z \sim 3.4 \pm 0.3$ starting in 2019. The foreground contaminations, zero spacing of interferometers, and small-scale noises of IM are the main factors that will downgrade the correlation. The loss of large-scale information makes it almost impossible to cross-correlate the IM surveys with other projected field surveys. After estimating the influence of these aspects for the correlation with the kSZ effect, we demonstrate how the tidal reconstruction algorithm [22–25] can increase the correlation.

The paper is organized as follows: Sec. II describes how to cross-correlate density fields with CMB temperature fluctuations (following Ref. [9]); Sec. III addresses the limits of 21 cm IM surveys and its influence on the correlations; Sec. IV demonstrates the scales of density and velocity fluctuations that contribute most in kSZ anisotropies; Sec. V summarizes the tidal reconstruction algorithm which reconstructs the missing large-scale modes; Sec. VI presents numerical results and expected S/N. We conclude in Sec. VII.

II. CROSS-CORRELATION OF DENSITY FIELDS WITH KSZ

The CMB temperature fluctuation caused by the kSZ effect is approximately a line-of-sight integral of the free electron momentum field:

$$\Theta_{\rm kSZ}(\boldsymbol{\theta}) \equiv \frac{\Delta T_{\rm kSZ}}{T_{\rm CMB}} = -\frac{1}{c}\int d\chi g(\chi) p_{\parallel}(\boldsymbol{\theta}, \chi), \quad (1)$$

where $\chi(z)$ is the comoving distance, $g(\chi) = e^{-\tau} d\tau/d\eta$ is the visibility function, τ is the optical depth of Thomson scattering, $p_{\parallel} = (1+\delta_e)v_{\parallel}$ is the free electron momentum field parallel to the line of sight, and $\delta_e = (\rho - \bar{\rho})/\bar{\rho}$ is the free electron overdensity, with $\bar{\rho}$ denoting the average density. It is assumed that electron overdensity δ_e is closely related to the baryon overdensity at $z < 2$; therefore, we simply use δ to denote both hereafter.

The direct correlation between kSZ and density fields vanishes due to the cancellation of positive and negative velocities; therefore, we follow the kSZ template method [9] to measure kSZ signal.

The peculiar velocity in a radial direction could be calculated from the linearized continuity equation:

$$v_z(\boldsymbol{k}) = iaHf\delta(\boldsymbol{k})\frac{k_z}{k^2}, \quad (2)$$

where a is the scale factor, $f = d\ln D/d\ln a$, $D(a)$ is the linear growth function, H is the Hubble parameter, and the indice z indicates the direction along LOS.

We generate the kSZ template of a selected redshift bin with the measured density field δ and the calculated radial velocity field v_z, following Eq. (1). Correlating the kSZ template with the CMB anisotropies selects the kSZ signal.

To quantify the tightness of the correlation between the kSZ template and the actual kSZ, we introduce a correlation coefficient r_ℓ:

$$r_\ell \equiv \frac{C_{\ell\,\rm tmpl,real}}{\sqrt{C_{\ell\,\rm tmpl}C_{\ell\,\rm real}}} \quad (3)$$

where $C_{\ell\,\rm tmpl,real}$ is the cross angular power spectrum.

III. CHALLENGES FOR 21 CM INTENSITY MAPPING

Given complete detection of density fluctuations, and following the procedures described in the previous section, we should be able to retrieve >90% of the kSZ signal from CMB at selected redshift bins [9]. However, 21 cm IM experiments are only sensitive to density fluctuations on certain scales because of several sources of noise:

(1) Foreground noises: IM uses all photons to map the density field. While gaining unprecedented survey speed, it leads to severe foreground contamination. The foregrounds, typically 3 orders of magnitude stronger than the signals, have complicated origins, ranging from galactic emission, extragalactic radio sources, and radio recombination lines to the noises from the telescopes [26,27]. The foreground will contaminate the signals of large-scale structures in the radial direction.

(2) Zero spacing problem of interferometers: Current 21 cm IM experiments are all carried out on interferometers—on the one hand, they are stable; on the other hand, the cross-correlations from different dishes have lower orders of noise than autocorrelations from a single dish. For CHIME-like facilities, with multiple beams installed on one dish, the calibration for cross-correlations between two beams of the same dish are complicated. Therefore, we only consider signals from cross-correlating different dishes for the rest of the paper. The minimum spacing between dishes, i.e., the shortest baseline of the interferometer, decides the largest angular scale it could probe. It results in an inner hole of small $k_\perp$ of a sampled density field in the Fourier space.

(3) Small-scale noises: The smallest-scale density fluctuations detectable in 21 cm IM experiments are jointly decided by the angular resolution of the facility, i.e., the longest baseline, receiver noise, and shot noise. For redshift 1, the receiver noise dominates. It gives an upper limit of the Fourier modes that we could detect.

The upper panel of Fig. 1 is an illustration of these effects in the density field obtained with 21 cm IM. Directly using it to correlate with the CMB map from Planck will only retrieve ∼10% of the underlying kSZ signal.

IV. IMPORTANT SCALES FOR KSZ

In the middle panel of Fig. 1, we compare the angular power spectrum of kSZ signals to those of primary CMB and of instrument noises from Planck at 217 GHz. The kSZ spectrum is based on the output of N-body simulations of two boxes of conformal distance 1 Gpc$/h$ centered at redshifts 1 and 2, respectively, as described in Sec. VI. With existing Planck [28] data, $\ell \sim 500$–2000 will be the visible window for the kSZ signal. The window could be extended to higher ℓs at the Simons Observatory [29] and CMB-S4 [30]. For this paper, we focus on $\ell \sim 500$–2000.

Fourier transforming Eq. (1), we obtain the kSZ anisotropies $\Theta(\boldsymbol{\ell})$ as a function of angular scale $\boldsymbol{\ell}$. Given that $g(\chi)$ in Eq. (1) is a slowly varying function, $\Theta(\boldsymbol{\ell})$ is proportional to the Fourier transform of the momentum field $p_\parallel(\boldsymbol{\ell}, 0)$ whose $k_z = 0$.

$$\Theta(\boldsymbol{\ell}) \propto p_\parallel(\boldsymbol{\ell}, 0) \propto \int d^3k \delta(\boldsymbol{\ell}/\chi(z) - \boldsymbol{k}_\perp, -k_\parallel) v_z(\boldsymbol{k}_\perp, k_\parallel). \quad (4)$$

where $\chi(z)$ denotes the comoving distance at redshift z.

Equation (4) shows that kSZ anisotropies come from the interaction of v_z and δ with $\boldsymbol{k}_\perp = \boldsymbol{\ell}/\chi$ separation in Fourier space. A demonstration of this convolution for kSZ $\ell \sim 500$–2000 is shown in Fig. 1.

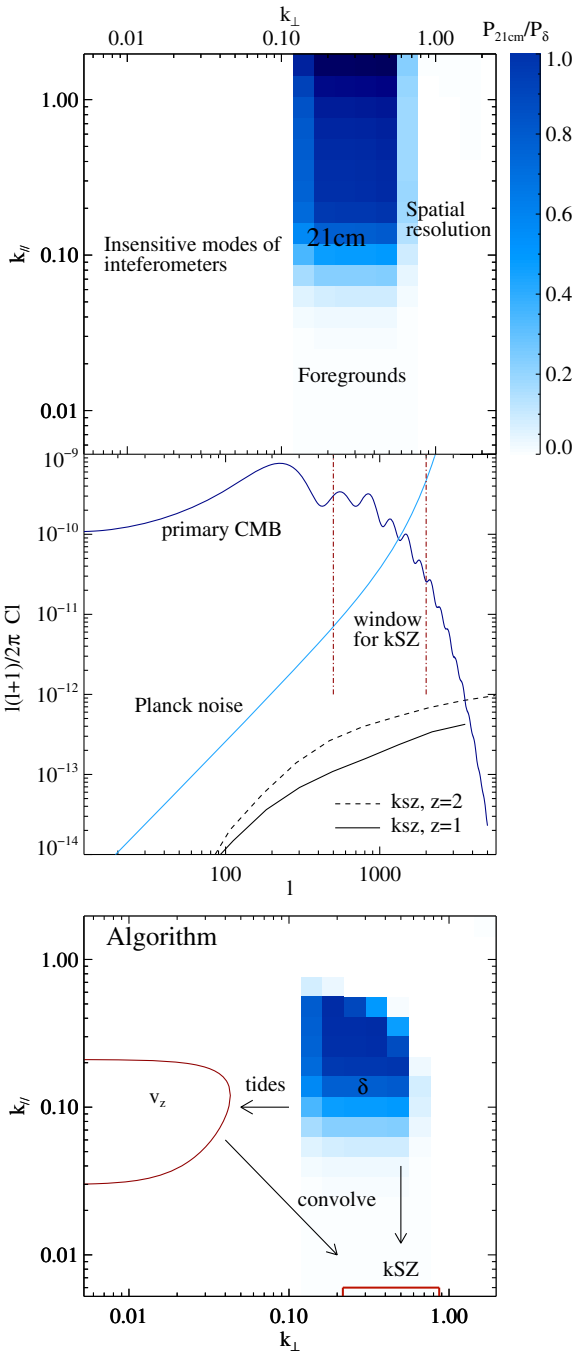

FIG. 1. (Top) The detectable scales of density fluctuations in 21 cm intensity mapping experiments with CHIME at redshift 1. (Middle) The angular power spectrum of kSZ signals from two boxes of conformal distance 1 Gpc$/h$ centered at redshift 1 and 2, respectively, as opposed to those of primary CMB and of instrument noises from Planck at 217 GHz. The kSZ spectrum is based on the output of N-body simulations described in Sec. VI. (Bottom) The generation of kSZ signals convolves density and velocity fields of different spatial scales. We use a tidal reconstruction algorithm to restore the contaminated large-scale modes in intensity mapping. The kSZ template is generated by convolving v_z calculated from a tidal reconstructed field and δ from 21 cm intensity mapping.

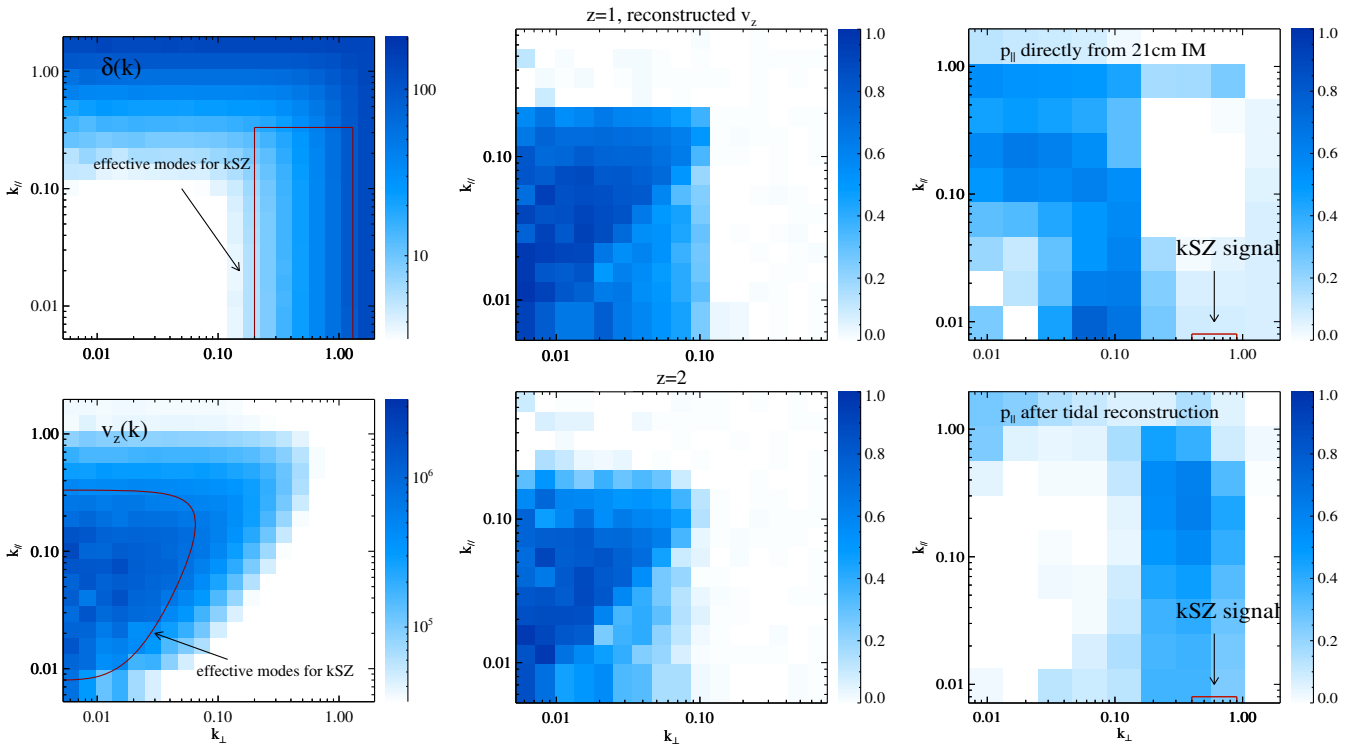

FIG. 2. (Left) The color represents the variances $2\pi^2\Delta^2 \equiv k^3P(k)$ of the complete density and velocity field at $z = 1$. It indicates the weights of different Fourier modes contributing to fields in real space. The modes that are essential for kSZ anisotropies at $\ell \sim$ 500–2000 are marked out. (Middle) The correlation coefficients between the tidal reconstructed $v_z^{\rm tide}$ and actual v_z at $z = 1, 2$, assuming the original field is collected by CHIME with high foregrounds. The v_z is linearly calculated from the density field; therefore, the panels also indicate the wave vector dependence of the correlation coefficient for the reconstructed density field $\delta^{\rm tide}$. (Right) The upper panel shows the correlation coefficient between momentum fields $p_\parallel = (1+\delta)v_z$ calculated from IM fields and the actual one. The lower panel shows the increased correlation after tidal reconstruction. The kSZ signal corresponds to $k_z \sim 0$ modes, for which $\ell \sim$ 500–2000 is marked out.

Although the convolution sums over all pairs of δ and v_z with a specific separation in Fourier space, the influence of each pair on the observed kSZ signals can be off by orders of magnitude depending on the power spectrum amplitudes of δ and v_z. In the left panels in Fig. 2, we show the variances $2\pi^2\Delta^2 \equiv k^3P(k)$ of density and velocity fields at redshift 1. Variance is an effective way to show contribution of different scales— the power spectrum $P(k)$ indicates the strength of $|\delta|$ or $|v_z|$ at scale k, and k^3 accounts for the integral in Eq. (4), which is a simple estimator for the space between k and $k + \Delta k$ in log-log plots.

Combining the two plots in the left panels of Fig. 2, we show that

(1) Within the range of $0.005 \lesssim k \lesssim 2\ h/\mathrm{Mpc}$, the power of the density fluctuations is mainly in small spatial scales, while the velocity field is large-scale dominant. Therefore, the kSZ signals we are interested in come from coupling of $\delta(\mathrm{large}k_\perp)$ with $v_z(\mathrm{small}k_\perp)$. In other words, for kSZ signal of all angular scales, the underlying large scale velocity field is almost identical. The angular scale of kSZ signal is closely related to the spatial scale of the density field.

(2) Although the kSZ signal is integrated through LOS, it contains information of density fluctuations up to few Mpc/h along LOS due to the interplay of two fields.

We mark the most relevant modes for generating the kSZ signal of $\ell \sim$ 500–2000 with red lines in Fig. 2.

The essential modes for density and velocity fields require completely different spatial resolutions. Since the velocity field is linearly constructed from the density field, an optimal survey should include essential modes of both fields. Comparing these essential modes with the modes resolvable in 21 cm IM (shown in Fig. 2, left panels, and Fig. 1, upper panel, respectively), we notice that while the effective modes for δ are partly resolved, the large-scale-dominated v_z is almost completely lost in the 21 cm IM. We attempt to recover these modes with cosmic tidal reconstruction [22,23].

V. COSMIC TIDAL RECONSTRUCTION

The density fluctuations on different scales interact under the gravitational interactions during nonlinear structure formation. The evolution of small-scale density fluctuations is modulated by the long-wavelength density

perturbations [23,31]. By studying the anisotropic tidal distortions of the local small-scale power spectrum, it is possible to solve the tidal field and hence the underlying large-scale structures [22–25].

The leading-order effect of the long-wavelength perturbation is described by the large-scale tidal field,

$$t_{ij} = \partial_i \partial_j \Phi_L - \nabla^2 \Phi_L \delta_{ij}/3, \tag{5}$$

where δ_{ij} is the Kronecker delta function and Φ_L is the long-wavelength gravitational potential. In gravitational lensing convention, the trace corresponds to magnification, while the traceless part is analogous to shear. Magnification is affected by intrinsic clustering and biasing and has different systematics from shear. In this paper, we concentrate on the shear. From Lagrangian perturbation theory, the local anisotropic matter power spectrum due to the tidal effect from large-scale density perturbations is

$$P(\boldsymbol{k},\tau)|_{t_{ij}} = P(k,\tau) + \hat{k}^i \hat{k}^j t_{ij}^{(0)} P(k,\tau) f(k,\tau), \tag{6}$$

where $\hat{k}^i$ is the unit vector, τ is the conformal time, $P(k,\tau)$ is the isotropic linear power spectrum, the superscript (0) denotes the initial time defined in perturbation calculation, and $f(k,\tau)$ is the tidal coupling function [23].

The tidal force tensor t_{ij} is symmetric and traceless and hence can be decomposed into five independent observables:

$$t_{ij} = \begin{pmatrix} \gamma_1 - \gamma_z & \gamma_2 & \gamma_x \\ \gamma_2 & -\gamma_1 - \gamma_z & \gamma_y \\ \gamma_x & \gamma_y & 2\gamma_z \end{pmatrix}. \tag{7}$$

The shear components of the tidal field induce different anisotropic distortions with different angular dependence to the local small-scale power spectrum. Therefore, from the angular dependence of the tidal shear distortions, we can solve for different components of t_{ij}. The reconstruction of gravitational tidal shear fields is described by the same formulation as the weak lensing reconstruction from CMB temperature fluctuations or a 21 cm intensity field [22–25]. The tidal shear fields are given by the quadratic fields of the small-scale density fluctuations, which are outer products of the filtered density fields,

$$\begin{aligned}
\hat{\gamma}_1(\boldsymbol{x}) &= [\delta_g^{w_1}(\boldsymbol{x})\delta_g^{w_1}(\boldsymbol{x}) - \delta_g^{w_2}(\boldsymbol{x})\delta_g^{w_2}(\boldsymbol{x})]/2, \\
\hat{\gamma}_2(\boldsymbol{x}) &= \delta_g^{w_1}(\boldsymbol{x})\delta_g^{w_2}(\boldsymbol{x}), \\
\hat{\gamma}_x(\boldsymbol{x}) &= \delta_g^{w_1}(\boldsymbol{x})\delta_g^{w_3}(\boldsymbol{x}), \\
\hat{\gamma}_y(\boldsymbol{x}) &= \delta_g^{w_2}(\boldsymbol{x})\delta_g^{w_3}(\boldsymbol{x}), \\
\hat{\gamma}_z(\boldsymbol{x}) &= [2\delta_g^{w_3}(\boldsymbol{x})\delta_g^{w_3}(\boldsymbol{x}) - \delta_g^{w_1}(\boldsymbol{x})\delta_g^{w_1}(\boldsymbol{x}) \\
&\quad - \delta_g^{w_2}(\boldsymbol{x})\delta_g^{w_2}(\boldsymbol{x})]/6,
\end{aligned} \tag{8}$$

where

$$\delta_g^{w_j}(\boldsymbol{k}) = i\hat{k}_j w(k)\delta_g(\boldsymbol{k}), \tag{9}$$

and $\delta_g \equiv \log(1+\delta)$. We take the logarithm to Gaussianize the density field [32]. In the long-wavelength limit and under the Gaussian assumption, the optimal window function for the minimum variance quadratic estimator can be constructed as

$$w(k) = \frac{\sqrt{P(k)f(k)}}{P_{\rm tot}(k)}, \tag{10}$$

where $P_{\rm tot}(k)$ is the total power spectrum measured from cosmological observations which includes both the signal and noise [23]. Note that $P(k)$ and $f(k)$ are again the isotropic linear power spectrum and tidal coupling function, respectively. As the tidal shear fields are related to second derivatives of the large-scale gravitational potential Φ_L, different components of t_{ij} can be combined to get the reconstructed large-scale density field

$$\delta^{\rm tide} \propto \nabla^2 \Phi = \frac{3}{2}\nabla^{-2}\partial_i \partial_j t_{ij}, \tag{11}$$

and in Fourier space,

$$\begin{aligned}
\delta^{\rm tide}(\boldsymbol{k}) \propto \frac{1}{2k^2}[&(k_1^2 - k_2^2)\gamma_1(\boldsymbol{k}) + 2k_1 k_2 \gamma_2(\boldsymbol{k}) + 2k_1 k_3 \gamma_x(\boldsymbol{k}) \\
&+ 2k_2 k_3 \gamma_y(\boldsymbol{k}) + (2k_3^2 - k_1^2 - k_2^2)\gamma_z(\boldsymbol{k})],
\end{aligned} \tag{12}$$

where the large-scale density information is from the convolution of a small-scale density field. More detailed steps are described in Ref. [23]. We make slight adjustments to use all five observables in t_{ij} rather than only γ_1 and γ_2 in the transverse plane.

We have also considered the influence of redshift distortion (RSD). Linearly, it is a change of the absolute value of $\delta(\boldsymbol{k})$ related to k_z, which is easy to correct. The nonlinear effect is difficult to remove, so we have include the RSD in the simulation to see the impact. In the simulation, we discard $\delta(\boldsymbol{k})$ with k_z greater than a cutoff scale $k_{z\,\rm max}$ considering the thermal noises of the receivers (parameters listed in Table I). Up to the cutoff scale the results barely change after including RSD. A detailed discussion about the RSD influence will be addressed in a following paper.

VI. SIMULATIONS

We run six N-body simulations, using the CUBEP^{3}M code [33], each evolving 1024^3 particles in a $(1.2\ {\rm Gpc}/h)^3$ box. Simulation parameters are set as follows: Hubble parameter $h = 0.678$, baryon density $\Omega_b = 0.049$, dark matter density $\Omega_c = 0.259$, amplitude of primordial

curvature power spectrum $A_s = 2.139 \times 10^{-9}$ at $k_0 = 0.05\ \mathrm{Mpc}^{-1}$, and scalar spectral index $n_s = 0.968$.

We output the simulated density fields δ at $z = 1, 2$ and apply filters to match the conditions of real 21 cm IM surveys:

$$\delta^{\mathrm{IM}}(\boldsymbol{k}) = \delta(\boldsymbol{k}) H(k_{\perp\max} - k_\perp) W(k_\parallel) H(\ell - \ell_{\min}) \quad (13)$$

where the Heaviside function $H(k_{\perp\max} - k_\perp)$ describes the angular resolution of the survey:

$$H(k_{\perp\max} - k) = \begin{cases} 1 & k \le k_{\perp\max} \\ 0 & k > k_{\perp\max}. \end{cases}$$

The high pass filter $W(k_\parallel)$ indicates the loss of information due to the foregrounds:

$$W(k_\parallel) = 1 - e^{k_\parallel^2 R_\parallel^2/2}.$$

For each redshift, we consider a high foreground case based on early observations [34] and a low foreground case from theoretical predictions [35]. The other Heaviside function $H(\ell - \ell_{\min})$ indicates the largest angular scale detectable with an interferometer,

$$H(\ell - \ell_{\min}) = \begin{cases} 0 & \ell \le \ell_{\min} \\ 1 & \ell > \ell_{\min}, \end{cases}$$

where $\ell_{\min}$ is determined by the length of the shortest baseline $B_{\min}$, $\ell_{\min} \sim 2\pi B_{\min}/(z+1)\lambda$. We conservatively choose a shortest baseline of ~20 m.

The parameters selected for two redshifts are listed in Table I.

We calculate the kSZ template following the procedure demonstrated in Fig. 1, lower panel. First, we solve for the missing large-scale modes of δ_{IM} with a tidal reconstruction algorithm. With the reconstructed large-scale density field δ^{tide}, we then calculate v_z^{tide} and cross-correlate it with δ^{IM} to get the kSZ template.

TABLE I. Parameters chosen to match the conditions of 21 cm IM. Note that $R_\parallel$ indicates the largest structure resolvable along the LOS after foreground removal; $k_{\perp\max}$ represents the spatial resolution; $\ell_{\min}$, decided by the shortest baseline, indicates the largest angular scale detectable with an interferometer.

	$z = 1$		$z = 2$	
	High foreground	Low foreground	High foreground	Low foreground
$R_\parallel$ Mpc/h	15	60	10	40
	CHIME	HIRAX	CHIME	HIRAX
$k_{\perp\max}$ h/Mpc	0.5	1.2	0.3	0.8
$k_{z,\max}$ h/Mpc	0.5		0.3	
$\ell_{\min}$	300		200	

Comparing the reconstructed v_z^{tide} field with the one directly output from simulations (Fig. 2, middle panels), we can see that the large-scale modes are well reconstructed. For the modes that contribute heavily to kSZ anisotropies (see Fig. 2, left bottom panel), more than 70% of the information is retrieved. The right panels of Fig. 2 show the increased information in the momentum field template after the tidal reconstruction. The kSZ signal corresponds to $k_z \sim 0$ modes of the momentum field, for which the correlation coefficient has an obvious increase at $\ell \sim 500$–2000.

The correlation coefficients between the recovered kSZ template and actual kSZ anisotropies from a certain redshift bin are presented in Fig. 3. At $z = 1$, the correlation coefficient can reach 0.6 before the small-scale noises start to dominate, while at $z = 2$, a correlation coefficient of 0.5 can be reached. The foreground level is still the dominate factor for the correlation coefficient. The correlation coefficient is reduced by 0.2 in the strong foreground case. Without tidal reconstruction, the cross-correlation

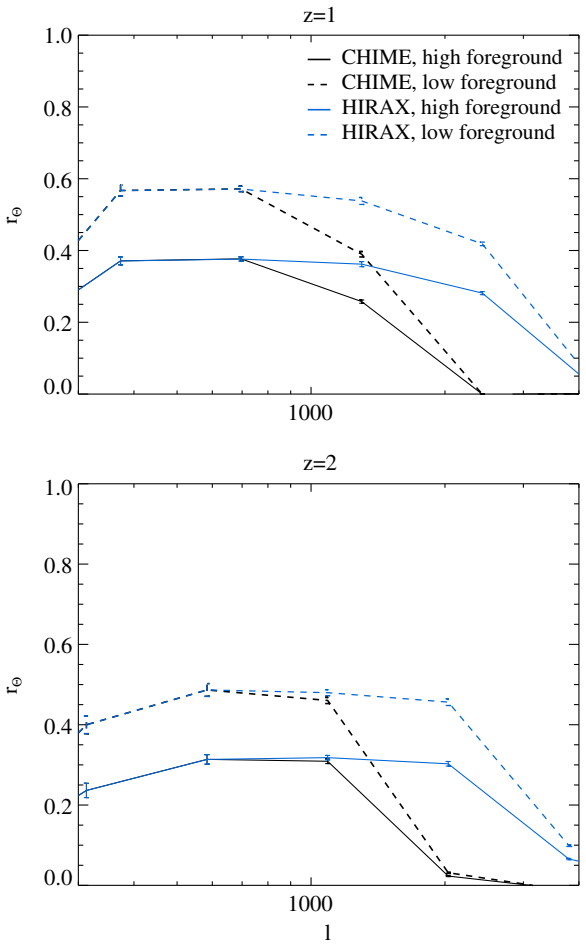

FIG. 3. The correlation coefficient r between kSZ anisotropies and kSZ templates generated from a 21 cm IM field. Forecasts for two instruments and different levels of foregrounds are calculated for $z = 1$ (above) and $z = 2$ (below).

will be ∼10%–15% for the low foreground case and $\lesssim$10% for the high foreground case. More than a factor of 2, up to a factor of 4, increase is seen after applying tidal reconstruction.

A. Signal to noise

The signal-to-noise ratio (S/N) for detecting kSZ effects can be estimated as [9]

$$\frac{S}{N} = \frac{C_\ell}{\Delta C_\ell} \simeq r\sqrt{(2\ell+1)\Delta l f_{\rm sky}}\sqrt{\frac{C_\ell^{\rm kSZ,\Delta z}}{C_\ell^{\rm CMB}+C_\ell^{\rm kSZ}+C_\ell^{\rm CMB,N}}}, \quad (14)$$

where $C_\ell^{\rm CMB}$ is the angular power spectrum of primary CMB, and $C_\ell^{\rm CMB,N}$ is the power spectrum of measurement noises. For $\ell \lesssim 2000$, the noises from the residual point sources are usually small compared to primary CMB. Thermal noise has the same white-noise power spectrum as point sources and can be adjusted to reflect the point-source contribution. On-sky derived noise measurements automatically contain this power, and for this study we assume the point-source power to be included in the thermal noise estimate. Here, $C_\ell^{\rm kSZ,\Delta z}$ is the kSZ signal from within a certain redshift bin, r is the correlation coefficient defined in Eq. (3), and $f_{\rm sky}$ is the percentage of sky area covered by both CMB and 21 cm IM surveys.

We calculate $C_\ell^{\rm CMB}$ using CAMB [36] and estimate $C_\ell^{\rm CMB,N}$ with Planck data [28] at 217 GHz. Note that $C_\ell^{\rm CMB,N} = (\sigma_{p,T}\theta_{\rm FWHM})^2 W_\ell^{-2}$, where $W_\ell = \exp[-\ell(\ell+1)/2\ell_{\rm beam}^2]$ is the smoothing window function, with $\ell_{\rm beam} = \sqrt{8\ln 2}/\theta_{\rm FWHM}$. Sensitivity per beam solid angle $\sigma_{p,T} = 8.7\ \mu{\rm K_{CMB}}$ and effective beam FWHM $\theta_{\rm FWHM} \sim 5'$. We assume sky coverage $f_{\rm sky} = 0.4$. Note that $C_\ell^{\rm kSZ,\Delta z}$ is calculated within two bins of size 1200 Mpc$/h$, centered at redshift 1 and 2, respectively.

The cumulative S/N for CHIME + Planck and HIRAX + Planck is shown in Fig. 4. The S/N at $z = 2$ is higher than $z = 1$ due to higher electron density. For CHIME + Planck, the resolution of CHIME determines the largest ℓ detectable, while for HIRAX + Planck, the resolution of Planck sets the limit. The kSZ signal is more prominent at larger ℓs due to the decreased strength of primary CMB; therefore, increasing the resolution of facilities will largely increase the cumulative S/N.

VII. RAMIFICATION

The kSZ anisotropies arise from the coupling of density and radial velocity fields of different spatial scales. Although the final anisotropies on CMB are 2D, they contain information on radial structure due to the coupling of the two fields. Different angular scales ℓ of kSZ track the density field of different spatial scales because the velocity field is large-scale dominant and contributes similarly to every ℓ. The strength of kSZ signals at various angular scales gives measurements of the baryon content and diffuseness.

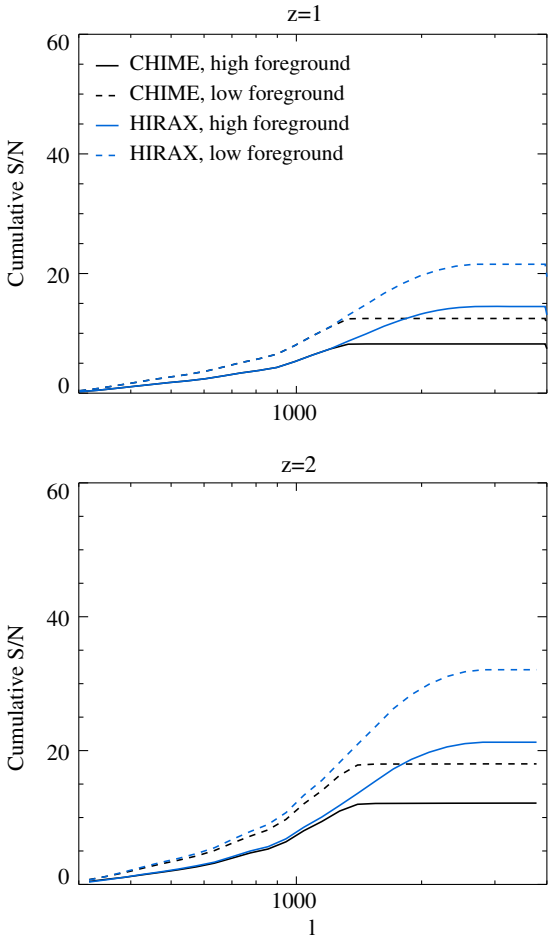

FIG. 4. Cumulative S/N for the detection of kSZ signals by cross-correlating CMB from Planck with density fields from CHIME or HIRAX with 40% sky coverage. The S/N is estimated for two redshift bins of 1 Gpc$/h$ centered at $z = 1$ and 2, respectively.

In this paper, we discuss the possibility of cross-correlating CMB with a 21 cm IM field as a probe for kSZ anisotropies. The 21 cm IM, with fast survey speed and accurate redshift information, is promising at detecting density fluctuations for large sky areas and high redshift. The biggest challenge for the cross-correlation is the loss of large-scale information in IM due to the foreground and interferometer zero spacing problem. To alleviate the problem, we reconstruct the missing large-scale modes in IM from their tidal influence on the small-scale density fluctuations. With $> 70\%$ of the relevant large-scale information retrieved, we are able to obtain correlation coefficients for kSZ and 21 cm fields of 0.6 for $z = 1$ and 0.5 for $z = 2$ in simulations. This is a significant increase from the ∼0.1 correlations obtained by directly using the foreground contaminated fields. For $\ell \sim 500$–2000, using

CHIME + Planck, a detection of $S/N \sim 20$ can be reached for $z \sim 0.8$–2.5, while for HIRAX + Planck, a $\sim 40\sigma$ detection can be expected. This S/N can be greatly increased with instruments of higher spatial resolution or by targeting at higher redshift where kSZ signals are more prominent, e.g., SPT-3G [37], Advanced ACTpol [38], Simons Observatory [29], CMB-S4 [30], Stage II Hydrogen IM experiment [39], etc.

We make several approximations in the paper. We use a dark matter field to assemble a HI field in the analysis, which enables us to work with simple N-body simulations. Careful treatment should include hydrodynamic simulations which take into account the baryonic effects (e.g., [40]). We use two boxes of 1.2 Gpc/h width output at $z = 1$, 2 to represent the density field of $z = 0.8$–2.5. This ignores the redshift evolution within each box. More careful work should include thinner boxes that output at different redshifts. We use a uniform weight when summing over different redshifts and angular scales. The S/N could be improved if proper weights are assigned [41]. We ignore the foreground wedge because it is not an intrinsic loss of information and is believed to be removable with a better understanding of instruments [42]. We use the distance between the closest receivers on nearby cylinders of CHIME as the shortest baseline and exclude ℓs smaller than the corresponding $\ell_{\rm min}$. In reality, given that the cylinders are placed closely together, CHIME is able to probe density fluctuations beyond the $\ell_{\rm min}$ we use; however, the sensitivity will quickly decrease as ℓ becomes less than the corresponding $\ell_{\rm min}$. Despite the simplifications, the current setups are sufficient to demonstrate the feasibility of cross-correlating CMB and 21 cm IM after tidal reconstruction to probe kSZ signals.

Cross-correlating the kSZ signal with 21 cm IM is promising due to its feasibility with near-term data. CHIME has started collecting data, and construction for HIRAX is underway. It is reasonable to expect our method to be testable within the next five years. This may foster understanding of stellar feedback at the scale of galaxy clusters and filaments and therefore the evolution of large-scale structures.

ACKNOWLEDGMENTS

We appreciate the comments from Philippe Berger on the manuscript. We appreciate Yu Yu for providing the N-body result. The simulations are performed on the SOSCIP Consortium's Blue Gene/Q computing platform. SciNet is funded by the Canada Foundation for Innovation under the auspices of Compute Canada; the Government of Ontario; the Ontario Research Fund—Research Excellence; and the University of Toronto. Research at the Perimeter Institute is supported by the Government of Canada through Industry Canada and by the Province of Ontario through the Ministry of Research & Innovation. The Dunlap Institute is funded through an endowment established by the David Dunlap family and the University of Toronto.

[1] R. Davé, R. Cen, J. P. Ostriker, G. L. Bryan, L. Hernquist, N. Katz, D. H. Weinberg, M. L. Norman, and B. O'Shea, Astrophys. J. **552**, 473 (2001).
[2] U.-L. Pen, Astrophys. J. **510**, L1 (1999).
[3] A. M. Sołtan, Astron. Astrophys. **460**, 59 (2006).
[4] R. A. Sunyaev and Y. B. Zeldovich, Comments Astrophys. Space Phys. **4**, 173 (1972).
[5] R. A. Sunyaev and I. B. Zeldovich, Mon. Not. R. Astron. Soc. **190**, 413 (1980).
[6] E. T. Vishniac, Astrophys. J. **322**, 597 (1987).
[7] M. Fukugita and P. J. E. Peebles, Astrophys. J. **616**, 643 (2004).
[8] N. Hand, G. E. Addison, E. Aubourg, N. Battaglia, E. S. Battistelli, D. Bizyaev, J. R. Bond, H. Brewington, J. Brinkmann, B. R. Brown *et al.*, Phys. Rev. Lett. **109**, 041101 (2012).
[9] J. Shao, P. Zhang, W. Lin, Y. Jing, and J. Pan, Mon. Not. R. Astron. Soc. **413**, 628 (2011).
[10] M. Li, R. E. Angulo, S. D. M. White, and J. Jasche, Mon. Not. R. Astron. Soc. **443**, 2311 (2014).
[11] J. C. Hill, S. Ferraro, N. Battaglia, J. Liu, and D. N. Spergel, Phys. Rev. Lett. **117**, 051301 (2016).
[12] S. Ferraro, J. C. Hill, N. Battaglia, J. Liu, and D. N. Spergel, Phys. Rev. D **94**, 123526 (2016).
[13] E. Schaan, S. Ferraro, M. Vargas-Magaña, K. M. Smith, S. Ho, S. Aiola, N. Battaglia, J. R. Bond, F. De Bernardis, E. Calabrese *et al.*, Phys. Rev. D **93**, 082002 (2016).
[14] C. Hernández-Monteagudo, Y. z. Ma, F.-S. Kitaura, W. Wang, R. Génova-Santos, J. Macías-Pérez, and D. Herranz, Phys. Rev. Lett. **115**, 191301 (2015).
[15] S. Lim, H. Mo, H. Wang, and X. Yang, arXiv:1712.08619.
[16] O. Doré, C. Hirata, Y. Wang, D. Weinberg, I. Baronchelli, A. Benson, P. Capak, A. Choi, T. Eifler, S. Hemmati *et al.*, arXiv:1804.03628.
[17] M. S. Madhavacheril, N. Battaglia, K. M. Smith, and J. L. Sievers, arXiv:1901.02418.
[18] K. Bandura, G. E. Addison, M. Amiri, J. R. Bond, D. Campbell-Wilson, L. Connor, J.-F. Cliche, G. Davis, M. Deng, N. Denman *et al.*, Proc. SPIE Int. Soc. Opt. Eng. **9145**, 914522 (2014).
[19] L. B. Newburgh, K. Bandura, M. A. Bucher, T.-C. Chang, H. C. Chiang, J. F. Cliche, R. Davé, M. Dobbs, C. Clarkson, K. M. Ganga *et al.*, Proc. SPIE Int. Soc. Opt. Eng. **9906**, 99065X (2016).

[20] Y. Xu, X. Wang, and X. Chen, Astrophys. J. **798**, 40 (2015).
[21] C. R. Subrahmanya, P. K. Manoharan, and J. N. Chengalur, J. Astrophys. Astron. **38**, 10 (2017).
[22] U.-L. Pen, R. Sheth, J. Harnois-Deraps, X. Chen, and Z. Li, arXiv:1202.5804.
[23] H.-M. Zhu, U.-L. Pen, Y. Yu, X. Er, and X. Chen, Phys. Rev. D **93**, 103504 (2016).
[24] H.-M. Zhu, U.-L. Pen, Y. Yu, and X. Chen, Phys. Rev. D **98**, 043511 (2018).
[25] S. Foreman, P. D. Meerburg, A. van Engelen, and J. Meyers, J. Cosmol. Astropart. Phys. 07 (2018) 046.
[26] T. Di Matteo, B. Ciardi, and F. Miniati, Mon. Not. R. Astron. Soc. **355**, 1053 (2004).
[27] K. W. Masui, E. R. Switzer, N. Banavar, K. Bandura, C. Blake, L.-M. Calin, T.-C. Chang, X. Chen, Y.-C. Li, Y.-W. Liao *et al.*, Astrophys. J. **763**, L20 (2013).
[28] R. Adam, P. A. R. Ade, N. Aghanim, M. Arnaud, M. Ashdown, J. Aumont, C. Baccigalupi, A. J. Banday, R. B. Barreiro *et al.* (Planck Collaboration), Astron. Astrophys. **594**, A8 (2016).
[29] P. Ade, J. Aguirre, Z. Ahmed, S. Aiola, A. Ali, D. Alonso, M. A. Alvarez, K. Arnold, P. Ashton *et al.* (Simons Observatory Collaboration), J. Cosmol. Astropart. Phys. 02 (2019) 056.
[30] K. N. Abazajian, P. Adshead, Z. Ahmed, S. W. Allen, D. Alonso, K. S. Arnold, C. Baccigalupi, J. G. Bartlett, N. Battaglia, B. A. Benson *et al.*, arXiv:1610.02743.
[31] F. Schmidt, E. Pajer, and M. Zaldarriaga, Phys. Rev. D **89**, 083507 (2014).
[32] D. H. Weinberg, Mon. Not. R. Astron. Soc. **254**, 315 (1992).
[33] J. Harnois-Déraps, U.-L. Pen, I. T. Iliev, H. Merz, J. D. Emberson, and V. Desjacques, Mon. Not. R. Astron. Soc. **436**, 540 (2013).
[34] E. R. Switzer, K. W. Masui, K. Bandura, L.-M. Calin, T.-C. Chang, X.-L. Chen, Y.-C. Li, Y.-W. Liao, A. Natarajan, U.-L. Pen *et al.*, Mon. Not. R. Astron. Soc. **434**, L46 (2013).
[35] J. R. Shaw, K. Sigurdson, M. Sitwell, A. Stebbins, and U.-L. Pen, Phys. Rev. D **91**, 083514 (2015).
[36] A. Lewis, A. Challinor, and A. Lasenby, Astrophys. J. **538**, 473 (2000).
[37] B. A. Benson, P. A. R. Ade, Z. Ahmed, S. W. Allen, K. Arnold, J. E. Austermann, A. N. Bender, L. E. Bleem, J. E. Carlstrom, C. L. Chang *et al.*, Proc. SPIE Int. Soc. Opt. Eng. **9153**, 91531P (2014).
[38] S. W. Henderson, R. Allison, J. Austermann, T. Baildon, N. Battaglia, J. A. Beall, D. Becker, F. De Bernardis, J. R. Bond, E. Calabrese *et al.*, J. Low Temp. Phys. **184**, 772 (2016).
[39] R. Ansari, E. J. Arena, K. Bandura, P. Bull, E. Castorina, T.-C. Chang, S. Foreman, J. Frisch, D. Green *et al.* (Cosmic Visions 21 cm Collaboration), arXiv:1810.09572.
[40] F. Villaescusa-Navarro, S. Genel, E. Castorina, A. Obuljen, D. N. Spergel, L. Hernquist, D. Nelson, I. P. Carucci, A. Pillepich, F. Marinacci *et al.*, Astrophys. J. **866**, 135 (2018).
[41] K. M. Smith, M. S. Madhavacheril, M. Münchmeyer, S. Ferraro, U. Giri, and M. C. Johnson, arXiv:1810.13423.
[42] A. Liu, Y. Zhang, and A. R. Parsons, Astrophys. J. **833**, 242 (2016).